ISSN 1063-7761, Journal of Experimental and Theoretical Physics, 2017, Vol. 125, No. 2, pp. 323–332. © Pleiades Publishing, Inc., 2017.
Original Russian Text © S.V. Komogortsev, V.A. Fel'k, R.S. Iskhakov, G.V. Shadrina, 2017, published in Zhurnal Eksperimental'noi i Teoreticheskoi Fiziki, 2017, Vol. 152, No. 2, pp. 379–390.

ORDER, DISORDER, AND PHASE TRANSITION IN CONDENSED SYSTEM

Micromagnetism in a Planar System with a Random Magnetic Anisotropy and Two-Dimensional Magnetic Correlations

S. V. Komogortsev[a], V. A. Fel'k[b]*, R. S. Iskhakov[a], and G. V. Shadrina[c]

[a] *Kirenskii Institute of Physics, Federal Research Center Krasnoyarsk Scientific Center, Siberian Branch, Russian Academy of Sciences, Akademgorodok, Krasnoyarsk, 660036 Russia*

[b] *Reshetnev Siberian State Aerospace University, Krasnoyarsk, 660014 Russia*

[c] *Siberian Federal University, Krasnoyarsk, 660074 Russia*

**e-mail: vlaf@sibsau.ru*

Received January 27, 2017

Abstract—The hysteresis loops and the micromagnetic structure of a ferromagnetic nanolayer with a randomly oriented local easy magnetization axis and two-dimensional magnetization correlations are studied using a micromagnetic simulation. The properties and the micromagnetic structure of the nanolayer are determined by the competition between the anisotropy and exchange energies and by the dipole–dipole interaction energy. The magnetic microstructure can be described as an ensemble of stochastic magnetic domains and topological magnetization defects. Dipole–dipole interaction suppresses the formation of topological magnetization defects. The topological defects in the magnetic microstructure can cause a sharper change in the coercive force with the crystallite size than that predicted by the random magnetic anisotropy model.

DOI: 10.1134/S1063776117070196

1. INTRODUCTION

Many functional elements of nanoelectronics, such as magnetic field sensors, spin waveguides, and spin rectifiers, contain magnetic layers of a nanometer thickness [1–3]. To optimize the magnetic properties of these layers, it is necessary to understand the relation between their properties and magnetic microstructure. The problem of a comprehensive theoretical description of thin films consists in the extremely high sensitivity of magnetic properties to structural defects in films. These defects include surface roughness, polycrystalline structure, crystallite boundaries, internal phase boundaries, dislocations, pores, and so on. The intense work of many scientific groups of technologists and material scientists that has been performed over the last decades led to the appearance of methods for controlling each of the well-known defects [1–6]. The influence of the polycrystalline structure of nanomaterials and, in particular, nanolayers on their properties has recently received the most study. It was found that the hysteretic properties of a material can be changed over very wide limits by changing the crystalline grain size [7–9].

The exchange and dipole–dipole interactions between nanocrystallites lead to magnetization correlations on the scales that can significantly exceed the grain size [10–15]. Along with random easy magnetization axis orientations, these magnetic correlations are the main attributes of the random magnetic anisotropy (RMA) model, which is now used to explain the magnetic properties of nanostructured materials [16, 17].

In the strong magnetic anisotropy limit (where magnetic anisotropy energy E_{an} is well above exchange energy E_{ex}), the approximation of independent crystallites holds true. This approximation was used to obtain a number of classic results concerning a magnetic hysteresis loop [18], the motion of magnetization to saturation [19], and ferromagnetic resonance [20, 21]. In terms of spatial scale, the condition of strong magnetic anisotropy can be expressed as $R_c/\delta \gg 1$, where R_c is the correlation radius of a local easy magnetization axis (i.e., a structural correlation radius proportional to the crystallite size) and $\delta = \sqrt{A/K}$ (where A is the exchange parameter and K is the anisotropy constant of a crystallite). Indeed, the ratio of spatial scales can be replaced by the ratio of the corresponding energies, $R_c/\delta = \sqrt{K/(A/R_c)^2} = \sqrt{E_{an}/E_{ex}}$; therefore, from $R_c/\delta \gg 1$ we have $E_{an}/E_{ex} \gg 1$.

In the weak magnetic anisotropy limit (where the magnetic anisotropy energy is well below the exchange energy, or $R_c/\delta \ll 1$), magnetization correlations extend to the scales that are significantly larger than R_c (crystalline grain size) [11, 15, 22–27]. This limit was applied to analytically solve the problems of a magnetization curve and the specific features of a micromag-

netic structure in high fields [11, 22–24, 26–28]. For the fields that are comparable with the coercive field, the development of an analytical theory of a magnetization curve encounters a number of difficulties related to the fact that the perturbation theory cannot be applied in this region and an irreversible change in micromagnetic states. However, the behavior of a material in low fields, which are comparable with the coercive field, is important for practical applications. Simple estimation formulas derived in terms of the RMA model are now used in the range of low fields [10, 11, 16, 17, 29, 30]. These formulas predict a power increase in the coercive force with R_c (or the crystallite size) and a decrease in the magnetic correlation radius with increasing R_c,

$$R_L \propto \frac{\delta^{4/(4-d)}}{R_c^{d/(4-d)}}, \quad H_c \propto K\left(\frac{R_c}{\delta}\right)^{2d/(4-d)}, \qquad (1)$$

where d is the dimension of the system.

It is obvious that a transition between the limiting cases of weak and strong anisotropy should occur at $R_c/\delta \sim 1$. The structural heterogeneity and the magnetic constants of the variety of real nanocrystalline alloys are such that the ratio $R_c/\delta \sim 1$ is valid for them (e.g., using constants A and K for bcc-Fe and $R_c =$ 21 nm, we obtain $R_c/\delta = 1$). To calculate the magnetization curves and the micromagnetic structures of such materials, neither the analytical results nor the scaling formulas of the RMA model can be used. Nevertheless, numerical results can be obtained by micromagnetic simulation in this case [31–40].

In this work, we performed micromagnetic calculations of the magnetic microstructure and the magnetization curves of a nanocrystalline layer with a random magnetic anisotropy and two-dimensional (2D) magnetization correlations.

The glass carbon films fabricated by widely used magnetron, plasma, and thermal sputtering and chemical and electrochemical deposition are polycrystalline; that is, they consist of a large number of crystalline grains. The magnetocrystalline anisotropy axes of grains are randomly oriented in the absence of an epitaxial coupling between a film and the substrate.

We now discuss the field of application of a model of a randomly oriented easy magnetization axis. Depending on the process of production, the following types of grain boundaries in nanocrystalline materials: coherent, semicoherent, and incoherent boundaries. In the case of coherent boundaries, the orientations of neighboring crystallites are not random. Here, the structural correlation length can exceed the crystallite size. However, orientation correlations become broken in large ensembles of crystallites on the scales that are significantly larger than the grain size, which can be detected by, e.g., X-ray diffraction. In the nanocrystalline alloys formed upon crystallization from an amorphous state, 1-nm-thick grain boundaries have an amorphous structure; as a result, the crystallographic orientations of neighboring crystallites are fully independent [41–43].

As a rule, one crystallite is present in a layer several nanometers thick along its normal [30, 44–46]. In this case, the correlations are two-dimensional since they propagate in the plane of a magnetic nanolayer. For magnets with 2D magnetization correlations, the RMA model predicts a quadratic increase in the coercive force with the crystallite size and a decrease in the magnetic correlation length in inverse proportion to the crystallite size (see Eq. (1) for $d = 2$).

Thin magnetic films are characterized by a significant contribution of dipole–dipole interaction to the total energy of the system. Unfortunately, to the best of our knowledge, there are no works that analytically take into account this contribution for films in the fields that are comparable with the coercive field for the case of a weak magnetic anisotropy.

The purpose of this work is to perform a micromagnetic simulation of a thin nanocrystalline layer in the magnetic fields that are comparable with the coercive field at various ratios of the exchange energy to the magnetic anisotropy of a crystallite. In addition, we studied the influence of dipole–dipole interaction on the magnetic properties and the magnetic microstructure of a nanolayer.

The films in which the anisotropy constant of a crystallite (K) significantly exceeds the maximum energy density of dipole–dipole interaction ($2\pi M_s^2$) can be considered as a practical example of the situation where dipole–dipole interaction may be neglected. These films include the films made of materials with a giant anisotropy constant, such as $CoFe_2O_4$ ($2\pi M_s^2 = 3 \times 10^5$ J/m^3, $K = 1.4 \times 10^6$ J/m^3) [49, 50] and an ordered CoPt solid solution ($2\pi M_s^2 = 7 \times 10^5$ J/m^3, $K = 4.7 \times 10^6$ J/m^3) [51, 52], and films with a low magnetization, such as Ni(P) nanolayers [47, 48, 53, 54]. As will be shown below, taking into account dipole–dipole interaction in a planar system effectively changes the number of magnetization components and, thus, causes new features due to a change in the topology of a system.

The structure of this article is as follows. In Section 2, we present the theoretical considerations and the parameters of the micromagnetic problem. In Section 3, we discuss the behavior of a hysteresis loop as a function of R_c/δ. The relation between the correlation properties of the system with its microstructure is described in Section 4. The problem of the influence of topological defects on this relation is discussed in Section 5.

2. MICROMAGNETIC SIMULATION

We define magnetization vector **M** as the sum N of magnetic moments $\boldsymbol{\mu}_j$ ($j = 1, ..., N$) in small volume dV determined by the position of a ferromagnetic particle **r**, namely,

$$\mathbf{M}(\mathbf{r}) \equiv \frac{1}{dV}\sum_{j=1}^{N}\boldsymbol{\mu}_j. \quad (2)$$

In micromagnetism, direction **M** can change continuously as a function of position [55]. Thus, a micromagnetic model implies a phenomenological description of a magnetic system as a continual medium. Here, magnetization is a continuous function of coordinates.

Each point in a continual medium is in an effective magnetic field, which can be expressed in terms of the total energy of the system E_{tot} as follows:

$$\mathbf{H}_{\text{eff}} \equiv -\mu_0^{-1}\frac{\partial E_{\text{tot}}}{\partial \mathbf{M}}, \quad (3)$$

where μ_0 is a magnetic constant. Then, the condition that determines the equilibrium magnetization vector orientation has the form

$$\mathbf{M}(\mathbf{r},t)\times\mathbf{H}_{\text{eff}}(\mathbf{r},t) = 0. \quad (4)$$

The total energy of a magnetic system is a function of magnetization. The total energy of a system in ferromagnetic materials can be represented as the sum of the following terms:

$$E_{\text{tot}} = E_{\text{exch}} + E_{\text{anis}} + E_{\text{mag}} + E_{\text{Zee}}. \quad (5)$$

These four terms are the exchange energy, the anisotropy energy, the magnetostatic or dipole–dipole energy, and the Zeeman energy (related to an external magnetic field). In an equilibrium stat, total energy (5) is minimal. Thus, each equilibrium state of the magnetic system corresponds to a local minimum of functional (5). In this work, we perform a micromagnetic simulation of a nanocrystalline layer with 2D magnetization correlations using the OOMMF software package [56]. The layer thickness was taken to be L_z = 10 nm. A correlation magnetization function was calculated on rectangular samples with lateral sizes of 1000 × 500 nm. Hysteresis loops were calculated for square samples with lateral sizes of 4000 × 4000 nm. The cell size was taken to be equal to the layer thickness (10 nm). Thus, the cell size in the plane is much smaller than the sample size (nanocrystallinity condition), and the thickness is equal to the cell size, which allows magnetization correlations to move only in the plate plane (2D magnetization correlations). The local uniaxial anisotropy constant in each cell was assumed to be $K = 10^5$ J/m^3 and the saturation magnetization of each cell was $M_s = 8.6 \times 10^5$ A/m. The easy magnetization axis of a cell was randomly oriented. The sample sizes are sufficient to neglect the influence of boundaries. For example, using additional tests, we found that taking into account closed boundary conditions does not change the results obtained without them. Positive exchange interaction constant A was chosen so that the required relations between the competitive energies of exchange and anisotropy were ensured. Note that the ratio of these energies reduced to a dimensionless form can be expressed in terms of the ratio of the characteristic scales R_c/δ as $KR_c^2/A = (R_c/\delta)^2$. From here on, we present our results as functions of R_c/δ and assume that R_c is equal to the cell size (10 nm). The dipole–dipole energy was calculated on the assumption that magnetization is constant in each cell [57, 58].

3. MAGNETIC HYSTERESIS

The hysteresis loops calculated for a magnetic field applied along axis x are substantially different for different values of R_c/δ for films with and without dipole–dipole interaction (Fig. 1). We now discuss the behavior of coercive force H_c and remanent magnetization M_r, which are important applied characteristics of a hysteresis loop. In Fig. 1, they are shown as the sections of a descending hysteresis loop branch, $M_r/M_s = f(H = 0,\ R_c/\delta,\ M/M_s)$ and $H_c = f(H,\ R_c/\delta,\ M/M_s = 0)$.

To estimate the average values and the dispersion of the coercive force and the remanent magnetization, we calculated several hysteresis loops at the same micromagnetic problem parameters for different random easy magnetization axes. Since a certain sample of easy magnetization axes is finite, the hysteresis loops calculated at the same micromagnetic problem parameters are different for different samples. These fluctuations in calculating noninteracting systems are on the order of $1/\sqrt{N}$, where N is the number of independent elements. In the exchange-uncoupled limit ($N = 1.6 \times 10^5$ in our case), the average magnetization fluctuation is 0.025%. When the exchange correlations are enhanced (or R_c/δ is decreased), the number of independent elements N decreases and fluctuations grow (Figs. 2, 3).

The coercive force calculated without regard for dipole–dipole interaction increases with R_c/δ (Fig. 2), and the following three segments can be distinguished in the dependence of H_c on R_c/δ. For a layer with R_c/δ higher than three, the shape of hysteresis loops approaches that in the Stoner–Wohlfarth model [18]. The coercive field tends toward $H_c = 0.96K/M_s$ (where M_s is the spontaneous magnetization) and the remanent magnetization tends toward $M_r/M_s = 0.5$ (Fig. 3). These values were calculated by Stoner and Wohlfarth for noninteracting particles, i.e., in the limit $R_c/\delta \to \infty$.

For a layer with R_c/δ from 0.5 to 1, the dependence of H_c on R_c/δ agrees with that predicted by the PMA model for 2D systems, $H_c \propto (R_c/\delta)^2$ [29, 30, 59].

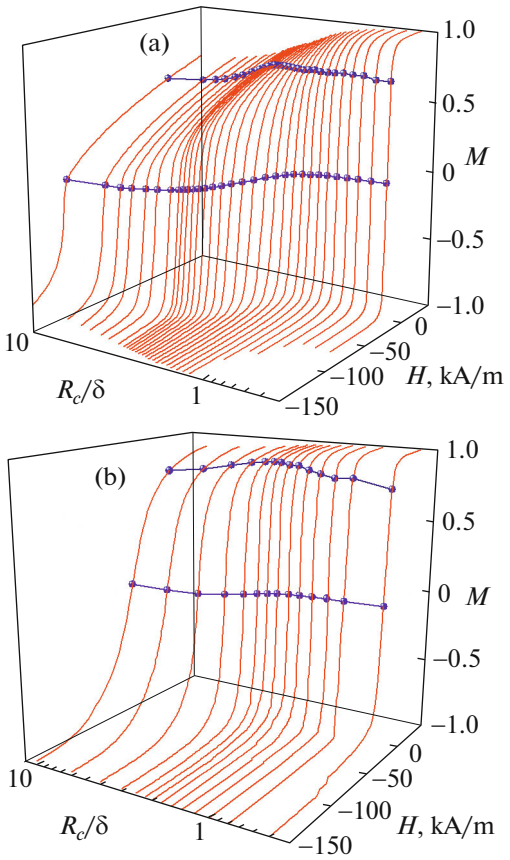

Fig. 1. (Color online) Hysteresis loops (a) without and (b) with allowance for dipole–dipole interaction.

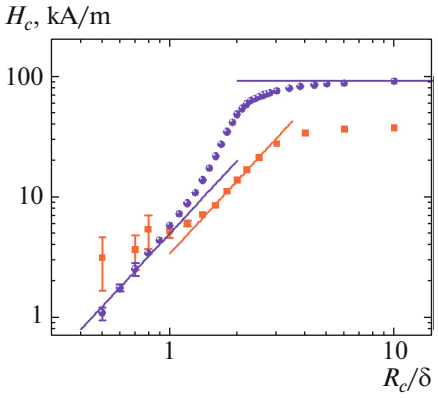

Fig. 2. (Color online) Coercive force in films with various R_c/δ ratios. (round symbols) Calculation without regard for dipole–dipole interaction and (square symbols) calculation with allowance for dipole–dipole interaction. The horizontal line is the limiting coercive force in the Stoner–Wohlfarth model. The slant lines illustrate power functions $H_c \propto R_c^2$.

Indeed, according to the RMA model we have $H_c \propto H_a/\sqrt{N}$. For the 2D case, this gives $N \propto (R_m/R_c)^2$ and $H_c \propto H_a(R_c/R_m) \propto H_a(R_c/\delta)^2$. When R_c/δ changes from 1 to 2, H_c increases with R_c/δ more strongly than quadratically. As will be discussed below, this behavior can be related to the formation of topological magnetic defects in the magnetic microstructure.

Remanent magnetization M_r/M_s increases with decreasing R_c/δ and becomes constant ($M_r/M_s \approx 0.72$) in the range $R_c/\delta < 2$ (Fig. 3). The absence of a dependence of the remanent magnetization on the ratio of the exchange and anisotropy energies (at $R_c/\delta < 2$) means the invariance of the static properties of the magnetic microstructure on this ratio. The increase in the remanent magnetization with decreasing R_c/δ can be explained as follows. In a zero field, the magnetic microstructure consists of stochastic magnetic domains. These domains are statistically independent and can be considered as a system of exchange-uncoupled particles. According to the Stoner–Wohlfarth model, if the easy magnetization axes of stochastic domains were be randomly oriented and the domains were be ideally magnetized (if the average magnetization of a domain was $M_r/M_s = 1$), the remanent magnetization would be $M_r/M_s \approx 0.5$. In real practice, the average magnetization of a stochastic domain is lower than unity; therefore, we would expect $M_r/M_s < 0.5$. The increase in the remanent magnetization to $M_r/M_s \approx 0.72$ can be explained by the appearance of texture in an ensemble of stochastic magnetic domains. Indeed, a system can decrease the anisotropy energy if stochastic domains are located at the sites where their averaged easy magnetization axes approach the direction of an external magnetic field. As a result, the remanent magnetization would increase. The limiting remanent magnetization is bounded by the average magnetization of a stochastic magnetic domain. The detected limiting value

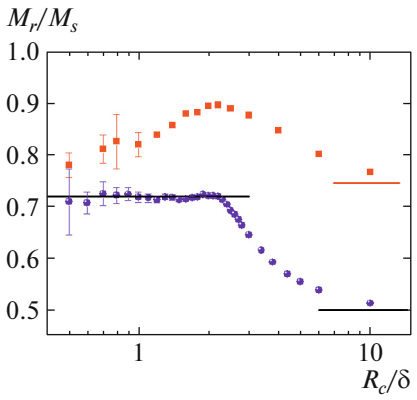

Fig. 3. (Color online) Remanent magnetization in films with various R_c/δ ratios. (round symbols) Calculation without regard for dipole–dipole interaction and (square symbols) calculation with allowance for dipole–dipole interaction. The horizontal lines illustrate the limiting remanent magnetizations at $R_c/\delta \gg 3$ and $R_c/\delta \ll 3$.

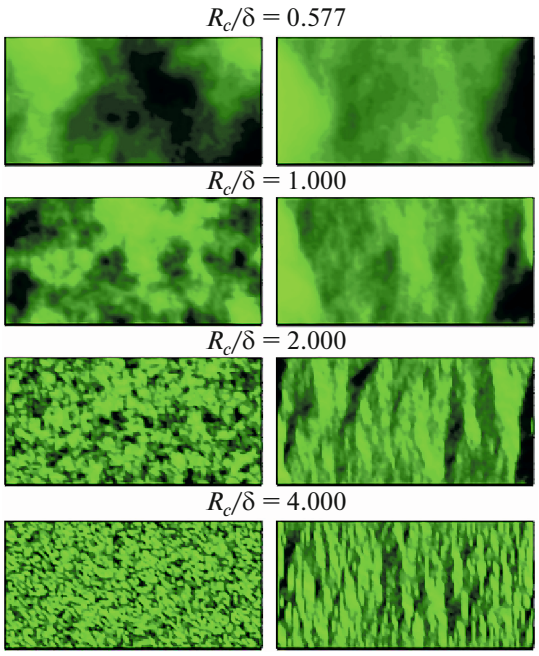

Fig. 4. (Color online) Nonuniformity of magnetization (for component m_y) in the remanent state at various R_c/δ ratios. (left column) Calculation without regard for dipole–dipole interaction and (right column) calculation with allowance for dipole–dipole interaction.

($M_r/M_s \approx 0.72$) is assumed to be the estimated average magnetization of a stochastic magnetic domain.

The dipole–dipole interaction leads to lower limiting coercive fields for high values of R_c/δ ($R_c/\delta > 3$) that those predicted by the Stoner–Wohlfarth model (Fig. 2). When the dipole–dipole interaction is taken into account, the dependence of H_c on R_c/δ exhibits a quadratic increase, which is predicted by the RMA model for $1.5 < R_c/\delta < 3$, and the coercive force then (at $R_c/\delta > 3$) levels off monotonically. At $R_c/\delta < 1$, the decrease in H_c slows down, which is clear if we use the relation $H_c \propto H_a(R_c/R_m)$. In the limit of low R_c/δ, the approaching of the maximum limiting value R_m should lead to the minimum limiting value of H_c. However, the maximum value R_m is limited by the sample size. The existence of this limitation is demonstrated by the calculations of the correlation magnetization radius given below (see Fig. 7 and the related discussions).

This limitation also causes an increase in the error of a numerical experiment when R_c/δ decreases. When R_m approaches the sample size, a small number of stochastic domains leads to the fact that the system cannot be averaged; i.e., the fluctuations of the physical parameters grow. The remanent magnetization for the calculation that takes into account a dipole–dipole interaction is higher than for the calculation when it is not taken into account and passes through a maximum at $R_c/\delta \approx 2.5$ when R_c/δ changes.

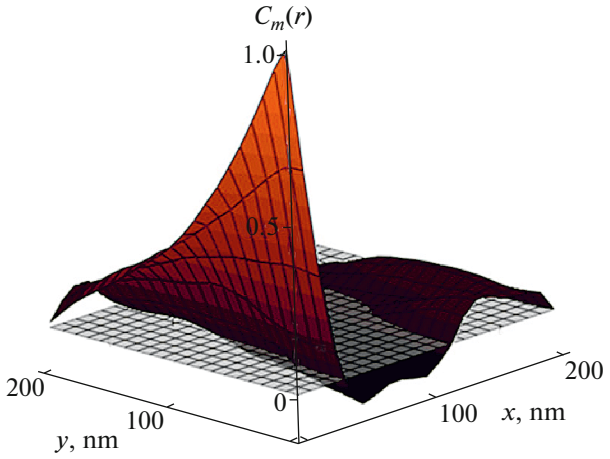

Fig. 5. (Color online) Correlation function of magnetization with allowance for dipole–dipole interaction.

4. STOCHASTIC MAGNETIC MICROSTRUCTURE. MAGNETIZATION CORRELATIONS

Figure 4 shows the distribution of magnetization projections in the state with remanent magnetization. At low R_c/δ, the magnetization is almost uniform for both versions, with and without dipole–dipole interaction (Fig. 4, $R_c/\delta = 0.577$). As R_c/δ increases, the nonuniformity becomes more pronounced: the uniform region size decreases and the magnetization fluctuation amplitude increases. At $R_c/\delta = 4$, the uniform magnetization region size becomes comparable with the cell size.

The nonuniformities of the magnetic microstructure calculated with allowance for dipole–dipole interaction are slightly extended along axis y, and the nonuniformities calculated without regard for this interaction are isotropic. The correlation functions of magnetization calculated as

$$C_m(r) = \langle m_y(x' + r)m_y(x')\rangle \qquad (6)$$

are decreasing and can be used to estimate the spatial lengths of magnetic of correlations and the dispersion of magnetization $C_m(0)$ (Figs. 5, 6). The anisotropic magnetization correlations in the system calculated with allowance for dipole–dipole interaction are characterized by an anisotropic correlation function (Fig. 5). Here, negative correlations are observed along x, which agrees with the numerical results and the experimental data obtained earlier for thin films [40, 60–62]. We will estimate the correlation properties for this case only for the correlations along x.

Magnetic correlation radius R_m is determined from functions $C_m(r)$ as the distance along which the correlations become half as much (Fig. 7). Several segments can be distinguished in the dependences of R_m on R_c/δ and of H_c on R_c/δ. For $R_c/\delta > 3$, R_m almost

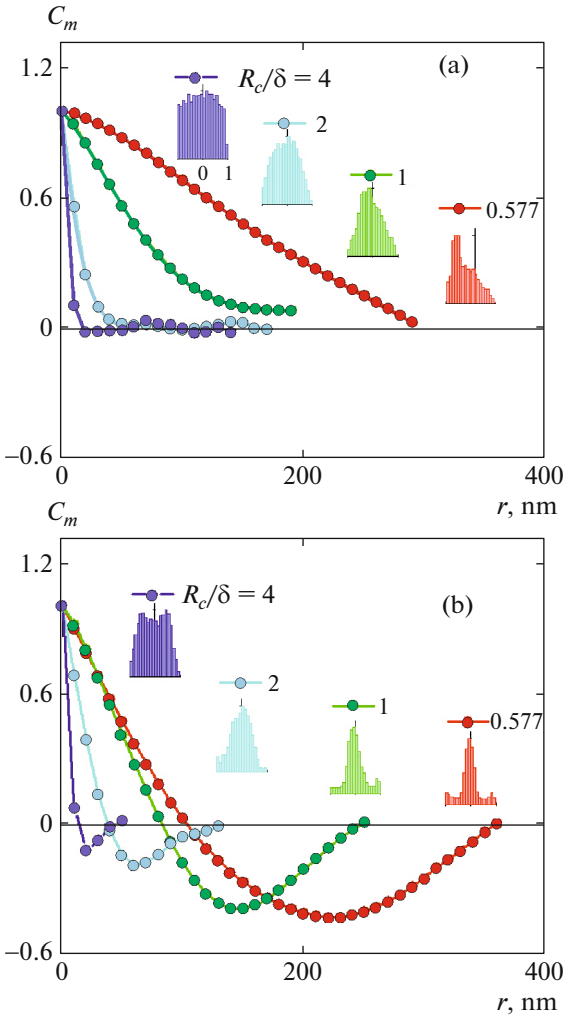

Fig. 6. (Color online) Correlation functions and the distribution of magnetization projections (m_y) (a) without and (b) with allowance for dipole–dipole interaction.

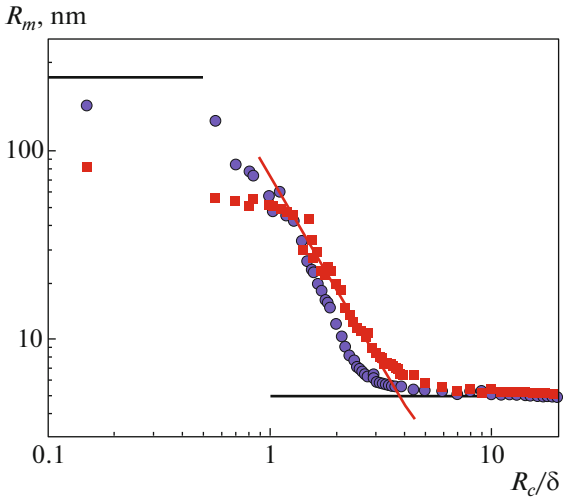

Fig. 7. (Color online) Magnetic correlation radius R_m vs. R_c/δ. (round symbols) Systems without dipole–dipole interaction and (square symbols) systems with dipole–dipole interaction. The straight line corresponds to the RMA model. The upper and lower horizontal straight lines indicate the sample size and half the cell size, respectively.

coincides with half the cell size. This result can easily be understood, since cells become exchange-uncoupled with each other. In this limit, the correlation function of magnetization repeats the correlation function of the easy magnetization axis of a cell [11, 28, 63]. In our micromagnetic model (where the easy magnetization axis of an individual cubic cell 10 nm in size is uniform), the correlations of an easy magnetization axis decrease with the distance as $C(r) = C(0)(1 - r/R_c)$ for $r < R_c$ and as $C(r) = 0$ for $r > R_c$. As follows from this formula, the correlation radius of the easy magnetization axis, which is determined as the distance along which the correlations become half as much, is $0.5R_c$, i.e., 5 nm. Indeed, the correlation radius of magnetization in Fig. 7 tends toward this value at $R_c/\delta > 3$.

In the calculations without regard for dipole–dipole interaction for a layer with $0.8 < R_c/\delta < 1.5$, the dependence of R_m on R_c/δ agrees with the prediction of the RMA model. According to the RMA model, we have $R_m \propto \delta^2/R_c = R_c(R_c/\delta)^{-2}$ for 2D systems with a Heisenberg (3D) magnetic moment [30, 59, 64]. The data in Fig. 7 at $0.8 < R_c/\delta < 1.5$ group well along a straight line at a slope of –2 in the log–log coordinates, which means that the dependence $R_m \propto (R_c/\delta)^{-2}$ holds true.

A deviation from the power dependence predicted by the RMA model is also observed at $1.5 < R_c/\delta < 3$, as in the dependence of the coercive force. As will be shown below, this deviation can be associated with a change in the correlation function of magnetization apart from the formation of topological magnetic defects in a magnetic structure. Indeed, the decrease in the correlation function with increasing distance is linear at high R_c/δ and is nonlinear at low R_c/δ (see Fig. 6). At $R_c/\delta < 0.8$, the points in Fig. 7 slowly approach a constant, which is caused by the finite size of the sample under study. Indeed, the upper limit in Fig. 7 (about 200 nm) is close to half the short side of a 500-nm rectangular plate. In this limit, the magnetization correlations are obviously bounded by this size from above.

The dipole–dipole interaction turned out not to affect the dependence of magnetization correlations on R_c/δ. However, the correlation radii in the range $R_c/\delta > 0.8$ are seen to exceed those in a sample without regard for dipole–dipole interaction. At $R_c/\delta < 0.8$, the situation is inverted: the correlation magnetization radii in a sample with dipole–dipole interaction turn out to be smaller. It is interesting that the dependence of R_m on R_c/δ with allowance for dipole–dipole inter-

action does not contain an additional region, which is similar to the third region in the dependence of R_m on R_c/δ without regard for dipole–dipole interaction (which was discussed above). The transition from the dependence $R_m \propto (R_c/\delta)^{-2}$ to constant R_m, which is bounded by the cell size from high values of R_c/δ, occurs in a very narrow R_c/δ range. Note that the data on the dependence of R_m on R_c/δ (Fig. 7) agree with the detected data on the dependence of H_c on R_c/δ (Fig. 2) in terms of the RMA model, $H_c \propto H_a/\sqrt{N} = H_a R_c/R_m$.

The magnetization projection distributions exhibit a more compact and symmetric scatter of the components with respect to zero with allowance for dipole–dipole interaction and low value of R_c/δ (see Fig. 6). At $R_c/\delta = 4$, a qualitative difference between the distributions shown in Figs. 6a and 6b is visible. The distribution of the components in Fig. 6a is almost uniform with respect to zero, and a specific feature in the form of a maximum near zero is observed in Fig. 6b. This result can be understood from the following considerations. In the case of calculations with allowance for dipole–dipole interaction, the magnetization loses one degree of freedom: magnetization projection m_z turns out to be close to zero, and m_x and m_y can fluctuate in the range from -1 to $+1$. Without regard for dipole–dipole interaction, all three projections can fluctuate the range from -1 to $+1$. The magnetization vectors for $R_c/\delta = 4$ without regard for dipole–dipole interaction can be distributed almost uniformly within a hemisphere, and a uniform distribution within a semicircle should take place with allowance for this interaction. It can easily be shown that the distribution of transverse magnetization projections in this case should be qualitatively different, as is seen in Figs. 6a and 6b.

5. TOPOLOGICAL DEFECTS IN A MAGNETIC MICROSTRUCTURE

Apart from smooth stochastic rotation of magnetization between various points in a sample, its magnetic microstructure also has specific points, so-called topological magnetic defects. Near a defect, the orientation of magnetization changes sharply. A vortex, hedgehog, or saddle magnetization structure can form in the vicinity of a defect. To estimate the influence of such defects on the magnetic properties, we calculate their number. It is difficult and ambiguous to distinguish individual defects visually against the background of a stochastic magnetization distribution; therefore, we used a quantitative characteristic, namely, a topological or skyrmion charge [65]

$$q = \frac{1}{4\pi M^3}\int \mathbf{M}\left(\frac{\partial \mathbf{M}}{\partial x}\times\frac{\partial \mathbf{M}}{\partial y}\right)dV. \qquad (7)$$

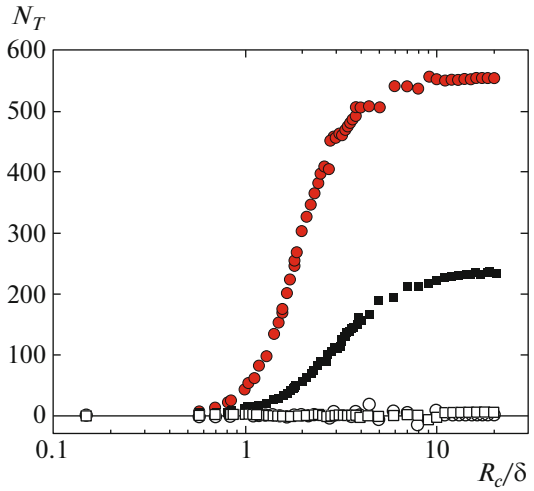

Fig. 8. (Color online) (open symbols) Topological charge q and (solid symbols) the number of topological defects N_T vs. R_c/δ. (circles) Calculation without regard for dipole–dipole interaction and (squares) calculation with allowance for dipole–dipole interaction.

The topological charge density (integrand in this expression) is a scalar alternating quantity. The values of q calculated for various values of R_c/δ fluctuate about zero (Fig. 8). A quantity that is proportional to the number of defects is obtained by integrating the modulus of the topological charge density,

$$N_T = \frac{1}{4\pi M^3}\int \left|\mathbf{M}\left(\frac{\partial \mathbf{M}}{\partial x}\times\frac{\partial \mathbf{M}}{\partial y}\right)\right| dV. \qquad (8)$$

As R_c/δ increases, the number of defects increases from zero to a constant at high values of R_c/δ (Fig. 8). This picture agrees with the evolution of the heterogeneity of a magnetic structure discussed for Figs. 4, 6, and 7. A decrease in the size of regions with a uniform magnetization orientation with increasing R_c/δ leads to an increase in the volume fraction of the boundaries between magnetic correlation volumes, where topological magnetic defects form.

Thus, we expect an increase in the number of topological magnetic defects with R_c/δ. Figure 8 can be used to qualitatively explain the deviation from the quadratic dependence of H_c on R_c/δ in the range $1.5 < R_c/\delta < 2$ in Fig. 2. At low R_c/δ, the number of defects is small, and the RMA model states that the quadratic dependence of H_c on R_c/δ is fully caused by the average magnetic anisotropy of a stochastic magnetic domain. The deviation from this dependence when R_c/δ increases in the range $1.5 < R_c/\delta < 2$ toward an increase can be related to the increase in the number of defects that is observed in Fig. 8. Indeed, the rotation of magnetization near a defect requires additional work to be done by a magnetic field, which should result in an increase in the magnetic hysteresis. For high R_c/δ, an ordered state of magnetization, against

the background of which a defect can be detected, is broken and the concept of a defect becomes inapplicable. The absence of such a deviation for the dependence of H_c on R_c/δ in the results of the calculation that takes into account dipole–dipole interaction can be associated with a substantially smaller number of topological defects forming in the system (Fig. 8). Indeed, dipole–dipole interaction effectively "turns off" the transverse component of magnetization. In our 2D system, this turning-off can be considered as a transition from the Heisenberg model to the so-called *xy* model, which is characterized by a two-component spin. According to [66], this approach should correspond to the transition from nonsingular topological structures with a weak metastability to singular structures with a strong metastability. The increase in the metastability means the growth of potential barriers that separate defectless and defect states. When moving along the limiting hysteresis loop from high fields to zero and, then, to the coercive field, we pass from a fully homogeneous state of magnetization to a heterogeneous state, which contains only topological defects. Since the nucleation of a defect in both cases (with and without dipole–dipole interaction) is caused by a random local anisotropy (which has the same absolute value), a smaller number of topological defects should form in the magnetic microstructure. The data in Fig. 8 support this consideration: the number of defects decreases substantially when dipole–dipole interaction is turned on. According to Imry and Ma [66, 67], the absolutely stable state in a system with a random magnetic anisotropy is characterized by the zeroth average projection of magnetization; therefore, a high remanent magnetization in the system with turned on dipole–dipole interaction also points to a higher metastability of this system (Fig. 3).

In our calculations, we used a random uniaxial anisotropy of neighboring crystallites for simplicity. We now discuss the applicability of our results to systems with a cubic anisotropy of crystallites. It is known that the shape of a hysteresis loop in a system of noninteracting crystallites with a cubic local symmetry differs from the shape of a loop for a system of uniaxial grains [18]. In particular, the Stoner–Wohlfarth model gives $H_c = 0.32H_a$ and $M_r/M_s = 0.83$ for a positive cubic anisotropy constant when a chaos is taken into account in the orientation of a local magnetic anisotropy [68]. We can also expect that a numerical investigation of the problem for a cubic local anisotropy would lead to a change in both the asymptotic values of H_c and M_r/M_s in the limit of exchange-uncoupled crystallites and a shift in the characteristic sizes at which the modes of exchange-coupled and exchange-independent crystallites are exchanged. Some of the obtained results are retained for ferromagnets with a cubic structure. For example, the exponents of the power dependences of the coercive force and the correlation magnetization radius are solely determined by the dimension of a system and the competition of a chaos in the orientation of a local easy magnetization axis, which breaks a long-range magnetic order and orders the influence of exchange interaction. Moreover, the qualitative difference between the behaviors of the coercive force and the number of topological defects in the presence and absence of dipole–dipole interaction in transient modes should be retained, since this difference is caused by a change in the topological class of the problem.

6. CONCLUSIONS

Using a micromagnetic simulation, we studied the hysteresis loops and the micromagnetic structure of a ferromagnetic nanocrystalline layer with a randomly oriented local easy magnetization axis and 2D magnetization correlations. The properties and the micromagnetic structure of the layer are determined by the competition between the anisotropy and exchange energies and also by the dipole–dipole interaction energy. The calculation without regard for dipole–dipole interaction for noninteracting crystallites results in the shape of a hysteresis loop that is predicted by the Stoner–Wohlfarth model. The correlation magnetization radius approaches a constant, which is comparable with the crystallite size. For a layer with strongly interacting crystallites, the dependences of the coercive force and the correlation magnetization radius on the reduced grain size or the structural correlation radius agree with the predictions of the RMA model for 2D systems, namely, a quadratic increase in the coercive force and a hyperbolic decrease in the correlation magnetization radius. For the intermediate case where the exchange correlation energy density is comparable with the local anisotropy constant, the coercive force increases with the reduced grain size more sharply than it is predicted by the RMA model. In the calculation with allowance for dipole–dipole interaction, this segment in the dependence of the coercive force on the reduced grain size is absent. The magnetic microstructure consists of an ensemble of magnetic correlation volumes, or stochastic magnetic domains. Topological magnetization defects form along the boundaries between the magnetic correlation volumes. As the reduced grain size increases, the number of defects increases from zero to a constant. Dipole–dipole interaction suppresses the formation of topological magnetization defects. The change in the number of these defects with the ratio of the anisotropy and exchange parameters agrees with a sharper change in the coercive force with the grain size than that predicted by the RMA model for the calculation without regard for dipole–dipole interaction and with the absence of this effect when dipole–dipole interaction is taken into account.

ACKNOWLEDGMENTS

This work was supported by the Russian Foundation for Basic Research, project no. 16-03-00256.

REFERENCES

1. G. T. Seng and B. A. J. Mansoor, Woodhead Publ. Ser. Electron. Opt. Mater., 312 (2012).
2. *Nanoelectronics and Information Technology,* Ed. by R. Waser, 3rd ed. (Wiley, New York, 2012).
3. *Micro- and Nanoelectronics: Emerging Device Challenges and Solutions*, Ed. by T. Brozek (CRC, Taylor and Francis Group, Boca Raton, FL, 2014).
4. *Nanoscale Magnetic Materials and Applications,* Ed. by J. P. Liu, E. Fullerton, O. Gutfleisch, and D. J. Sellmyer (Springer Science, New York, 2009).
5. J. P. Volkerts, *Magnetic Thin Films: Properties, Performance, and Applications* (Nova Science, New York, 2011).
6. H. S. Nalwa, *Handbook Thin Film Materials*, Vol. 1: *Deposition and Processing of Thin Films* (Academic, New York, 2002).
7. G. Herzer, in *Handbook of Magnetism and Advanced Magnetic Materials*, Ed. by H. Kronmuller and S. Parkin (Wiley, Chichester, UK, 2007).
8. G. Herzer and L. K. Varga, J. Magn. Magn. Mater. **506**, 215 (2000).
9. G. Herzer, J. Magn. Magn. Mater. **294**, 99 (2005).
10. R. Alben, J. J. Becker, and M. C. Chi, J. Appl. Phys. **49**, 1653 (1978).
11. E. M. Chudnovsky, W. M. Saslow, and R. A. Serota, Phys. Rev. B **33**, 251 (1986).
12. R. Skomski, J. Phys.: Condens. Matter **15**, R841 (2003).
13. R. S. Iskhakov, S. V. Komogortsev, Z. M. Moroz, and E. E. Shalygina, J. Exp. Theor. Phys. Lett. **72**, 603 (2000).
14. R. S. Iskhakov, V. A. Ignatchenko, S. V. Komogortsev, and A. D. Balaev, J. Exp. Theor. Phys. Lett. **78**, 646 (2003).
15. A. Michels, R. Viswanath, J. Barker, and R. Birringer, and J. Weissmüller, Phys. Rev. Lett. **91**, 267204 (2003).
16. G. Herzer, Acta Mater. **61**, 718 (2013).
17. R. S. Iskhakov and S. V. Komogortsev, Phys. Met. Metallogr. **112**, 666 (2011).
18. E. C. Stoner and E. P. Wohlfarth, Phil. Trans. R. Soc. A **240**, 559 (1948).
19. N. S. Akulov, Z. Phys. **69**, 822 (1931).
20. E. Schlömann, J. Phys. Radium **20**, 327 (1959).
21. E. Schlömann, Phys. Rev. **182**, 632 (1969).
22. H. Hoffmann, Phys. Status Solidi **5**, 187 (1964).
23. H. Hoffmann, J. Appl. Phys. **35**, 1790 (1964).
24. V. A. Ignatchenko, Sov. Phys. JETP **27**, 162 (1968).
25. G. Herzer, IEEE Trans. Magn. **25**, 3327 (1989).
26. K. J. Harte, J. Appl. Phys. **39**, 1503 (1968).
27. K. J. Harte, J. Appl. Phys. **37**, 1295 (1966).
28. V. A. Ignatchenko, R. S. Iskhakov, and G. V. Popov, Sov. Phys. JETP **55**, 878 (1982).
29. G. Herzer, Mater. Sci. Eng. A **133**, 1 (1991).
30. R. S. Iskhakov, S. V. Kolmogortsev, A. D. Balaev, and L. A. Chekanova, JETP Lett. **72**, 304 (2000).
31. S. V. Komogortsev and R. S. Iskhakov, Phys. Solid State **47**, 495 (2005).
32. H. Kronmüller, R. Fischer, R. Hertel, and T. Leineweber, J. Magn. Magn. Mater. **175**, 177 (1997).
33. A. A. Ivanov, V. A. Orlov, and G. O. Patrushev, Phys. Met. Metallogr. **102**, 485 (2006).
34. A. A. Ivanov, V. A. Orlov, and G. O. Patrushev, Phys. Met. Metallogr. **103**, 219 (2007).
35. R. Fischer and H. Kronmüller, J. Magn. Magn. Mater. **191**, 225 (1999).
36. I. R. McFadyen and I. A. Beardsley, J. Appl. Phys. **67**, 5540 (1990).
37. R. C. Giles and M. Mansuripur, J. Appl. Phys. **69**, 4712 (1991).
38. J. J. Miles and B. K. Middleton, J. Magn. Magn. Mater. **95**, 99 (1991).
39. B. A. Belyaev, A. V. Izotov, and A. V. Leksikov, Phys. Solid State **52**, 1664 (2010).
40. D. Berkov and N. Gorn, Phys. Rev. B **57**, 14332 (1998).
41. H. Gleiter, Prog. Mater. Sci. **33**, 223 (1989).
42. A. I. Gusev and A. A. Rempel, *Nanocrystalline Materials* (Fizmatlit, Moscow, 2001; Cambridge Int. Sci., Cambridge, 2004).
43. R. A. Andrievskii and A. M. Glezer, Phys. Met. Metallogr. **89**, 83 (2000).
44. M. C. Contreras, J. F. Calleja, R. Matarranz, B. Presa, J. A. Corrales, and G. Pan, J. Appl. Phys. 99, 08F110 (2006).
45. J. Echigoya and R. Yue, J. Mater. Sci. **40**, 3209 (2005).
46. R. S. Iskhakov, S. V. Komogortsev, A. D. Balaev, and L. A. Chekanova, Tech. Phys. Lett. **28**, 725 (2002).
47. K. Hüller, G. Dietz, R. Hausmann, and K. Kölpin, J. Magn. Magn. Mater. **53**, 103 (1985).
48. A. Berrada, F. Gautier, M. F. Lapierre, B. Loegel, P. Panissod, C. Robert, and J. Beille, Solid State Commun. **21**, 671 (1977).
49. N. Ranvah, Y. Melikhov, D. C. Jiles, J. E. Snyder, A. J. Moses, P. I. Williams, and S. H. Song, J. Appl. Phys. 103, 07E506 (2008).
50. M. Grigorova, H. J. Blythe, V. Blaskov, V. Rusanov, V. Petkov, V. Masheva, D. Nihtianova, L. M. Martinez, J. S. Muñoz, and M. Mikhov, J. Magn. Magn. Mater. **183**, 163 (1998).
51. S. V. Komogortsev, R. S. Iskhakov, A. A. Zimin, E. Y. Filatov, S. V. Korenev, Y. V. Shubin, N. A. Chizhik, G. Y. Yurkin, and E. V. Eremin, Appl. Phys. Lett. **103**, 152404 (2013).
52. P. Andreazza, V. Pierron-Bohnes, F. Tournus, C. Andreazza-Vignolle, and V. Dupuis, Surf. Sci. Rep. **70**, 188 (2015).
53. J. Carini, S. Nagel, L. Varga, and T. Schmidt, Phys. Rev. B **27**, 7589 (1983).
54. J. Schneider and H. Wiesner, Phys. Status Solidi **29**, K25 (1975).
55. W. F. Brown, *Micromagnetics* (Interscience, New York, 1963).

56. M. J. Donahue and D. G. Porter, Interagency Report NISTIR No. 6376 (Natl. Inst. Standards Technol., Gaithersburg, MD, 1999).
57. A. Aharoni, J. Appl. Phys. **83**, 3432 (1998).
58. A. J. Newell, W. Williams, and D. J. Dunlop, J. Geophys. Res. Solid Earth **98**, 9551 (1993).
59. R. Skomski, J. Phys.: Condens. Matter **15**, R841 (2003).
60. J. N. Chapman, S. McVitie, and S. J. Hefferman, J. Appl. Phys. **69**, 6078 (1991).
61. P. ten Berge, J. C. Lodder, R. Plössl, and J. N. Chapman, J. Magn. Magn. Mater. **120**, 362 (1993).
62. T. Suzuki, Phys. Status Solidi **37**, 101 (1970).
63. V. A. Ignatchenko and R. S. Iskhakov, Izv. Akad. Nauk SSSR, Ser. Fiz. **44**, 1434 (1980).
64. L. Thomas, J. Tuaillon, J. P. Perez, V. Dupuis, A. Perez, and B. Barbara, J. Magn. Magn. Mater. **437**, 140 (1995).
65. A. A. Belavin and A. M. Polyakov, JETP Lett. **22**, 245 (1975).
66. T. C. Proctor, D. A. Garanin, and E. M. Chudnovsky, Phys. Rev. Lett. **112**, 097201 (2014).
67. Y. Imry and S. K. Ma, Phys. Rev. Lett. **35**, 1399 (1975).
68. S. I. Smirnov and S. V. Komogortsev, J. Magn. Magn. Mater. **320**, 1123 (2008).

Translated by K. Shakhlevich